Performance of A Triboelectric Nanogenerator Utilising Coconut Husk Layer

Muhammad Aqmal Saparin[*]
Department of Electrical Engineering, College of Engineering
Universiti Tenaga Nasional (UNITEN), Jalan IKRAM-UNITEN,
43000 Kajang, Selangor, MALAYSIA
[*]*aqmal.saparin@uniten.edu.my*

Hanim Salleh, Chong Kok Hen
Institute of Sustainable Energy, Universiti Tenaga Nasional, MALAYSIA

Siti Nur Aliah Amnuruddin
Department of Mechanical Engineering, College of Engineering,
Universiti Tenaga Nasional, MALAYSIA

ABSTRACT

Triboelectric nanogenerators, known as TENGs, offer great potential as versatile energy harvesting devices. In recent years, there has been a rise in TENG designs that prioritize compatibility with sustainable biomaterials, leading to new possibilities in green technology. The novelty of this work lies in its pioneering exploration of utilizing sustainable biomaterials, particularly coconut husk, within the field of Tribo-electric nanogenerators (TENGs). This study focuses on evaluating and characterizing coconut husk as TENG material considering factors such as rotational speed, vane count, and coarseness, all of which influence the output potential of the B-TENG. The B-TENG model employed in this research operates on a rotational sliding mode, featuring a biobased material layer of coconut husk, a layer of PTFE, and copper as electrodes. The B-TENG has a diameter of 100 mm with varying vane configurations (3-vane, 4-vane, and 5-vane). The sliding mode demonstrated impressive versatility, yielding output voltages spanning from 0.73 V to 4.0 V across rotational speeds of 200 RPM to 1400 RPM. Remarkably, the 5-vane fine-grained coconut husks achieved a maximum power of 121.10 mW at 10 Ohm and a power density of 3.84 mW/cm^2. This research carries global significance, contributing to the advancement of

ISSN 1823-5514, eISSN 2550-164X
Received for review: 2023-11-20
Accepted for publication: 2024-04-25
Published: 2024-09-15

https://doi.org/10.24191/jmeche.v21i3.27350

energy harvesting technology. Its applications range from harnessing the motion of human bodies to rotating machineries in any industry.

Keywords: *Bio-Based Triboelectric Nanogenerator; Biomaterial; Self-Powered Sensor; Energy Harvesting*

Introduction

Until recently, the main mechanisms used for mechanical energy harvesting techniques developed over the last few decades were electromagnetic induction, piezoelectric, and electrostatic effects [1]-[2]. Triboelectric nanogenerators utilize the triboelectric effect to generate useable electricity, which is then used to power small circuits and devices. Triboelectric nanogenerators (TENG) use the concepts of contacting electrification and electrostatic production from mechanical energy to electrical energy [3]. Triboelectric nanogenerators, utilizing transducer elements, can harness diverse environmental energy forms, enabling self-sustained operation independent of conventional energy sources; characterized by a straightforward design, cost-effectiveness, compact dimensions, robust biocompatibility, and elevated instantaneous power density, they have emerged as a compelling auxiliary technology in the realm of Internet of Things [4]. Triboelectric Nanogenerators (TENGs) have several benefits, including high conversion efficiency, low cost, great output power, and easy production [5]-[6]. The generation of tribo-charges during contact and separation arises from the characteristics of the materials in contact and typically exhibits opposite polarities, as per the conventional perspective [7]-[8]. The materials create an electrical potential within the system when they come into contact and then separate. The self-powering capability can be achieved by harvesting ambient environmental energy readily available in the natural ecosystem by converting mainly mechanical energy to electricity [9]. This process, known as electrostatic induction, involves the transfer of electrons from one electrode to the other through the external load to equalize the potential difference. The electrostatic charges formed as a capacitive energy unit when two distinct triboelectric surfaces are separated played a crucial role in the early development of electrostatic generators. The combination of this triboelectric effect with electrostatic induction is key to the operation of TENGs [10]. Capable of transforming micro-/nano-scale mechanical energy into electrical energy utilizing the principles of both piezoelectricity and triboelectricity [11].

The novelty of this work lies in its pioneering exploration of utilizing sustainable biomaterials, particularly coconut husk, within the field of Triboelectric nanogenerators (TENGs). This represents a significant departure from traditional TENG designs that often rely on non-renewable or less eco-

friendly materials. By leveraging Malaysia's abundant resources in biomaterials, the study showcases the potential of incorporating locally available, renewable resources into energy harvesting technologies. The focus on coconut husk as a key component in the development of a biobased Triboelectric nanogenerator (B-TENG) underscores the commitment to sustainability and environmental responsibility. Coconut husk, an agricultural byproduct, offers a compelling alternative to conventional materials, tapping into a rich yet underutilized resource stream. Biomaterials sourced from nature, known for their eco-friendly nature, lack of toxicity, ease of acquisition, and abundance, have become indispensable materials across various industries [12]. Material improvement, structural optimization, surface modification, and other methods have proved to be effective in improving the output performance of TENG [13]. To date, a plethora of bio-based materials, including cellulose, chitin-chitosan, polylactic acid, and polybutylene succinate, have been recognized for their excellence, with a particular emphasis on cellulose and its derivatives as crucial biomasses [14]. Hence, in this work, the utilization of pollutant waste toward energy conversion has been proposed by fabricating a sliding TENG from recycled coconut waste. The coconut husk is composed of 30% fiber and 70% with high lignin and phenolic content [15]. Lignin molecules have proven to be highly effective tribopositive nanofillers, significantly enhancing the triboelectric charge density in biopolymer-based Triboelectric Nanogenerators (TENG) [16]-[17]. Coconut stands as Malaysia's fourth most crucial agricultural commodity, following palm oil, rubber, and paddy, holding the distinction of being the country's oldest industrial crop, contributing RM70.1 million, equivalent to 0.06% of Malaysia's agricultural export revenue [18]. To meet both small- and large-scale energy needs, energy harvesting, and storage technologies play an essential role in society. Although current battery technologies meet current needs, their short life, frequent recharging, and toxicity keep them from being widely used. Harnessing mechanical energy as an environmentally friendly method holds great promise, playing a pivotal role in energizing wearable electronics, sensor networks within the Internet of Things (IoTs), and artificial intelligence (AI) systems [19]-[21].

This research endeavors to characterize a Coconut husk-based Bio-Based Triboelectric Nanogenerator (B-TENG) by optimizing parameters such as the number of vanes and material coarseness to attain the highest output voltage, with a comprehensive examination of the finalized design's performance, including assessments of maximum voltage output, maximum power output, and power density.

Materials and Methods

The experimental materials and methods encompass various critical aspects of triboelectric nanogenerator (TENG) research, including material selection, fabrication, measurement procedures, characterization methods, and overall methodology. The most significance of choosing natural materials lies in their abundance, sustainability, low cost, biocompatibility, and durability, all of which directly impact TENG performance. This experiment will use the coconut husk as material selection. Precision in fabrication is paramount to ensure consistent device performance and desired structural attributes. Techniques such as micro/nanofabrication, printing, and assembly processes play pivotal roles in shaping TENG architectures. Accurate measurement and characterization techniques are indispensable for evaluating TENG performance metrics such as output voltage, current, power, and charge density. Ongoing research endeavors aim to enhance TENG functionality and performance through innovative methodologies, including novel approaches for energy harvesting, device integration, and system optimization.

Materials and fabrication

Based on Figure 1, the fabrication design and detailed layers are presented for the sliding mode of the B-TENG. The sliding mode comprises two sides: the stator and the rotor, each composed of copper and acrylic materials. The rotor layer of the B-TENG features side-facing Polytetrafluoroethylene (PTFE) on the copper plate, serving as the conductor and attached to an acrylic substrate. On the stator side, a layer of coconut husk is affixed to the copper plate, with acrylic acting as the substrate. The coconut husks were ground in a blender for 5 minutes to 10 minutes to obtain a powder-like consistency. To create a smooth contact between the PTFE surfaces, the coconut husk was immersed in a PDMS solution and left to dry, forming a plastic layer. The fabrication process for the rotary sliding-mode B-TENG's bottom plate supporting layer involved evaluating two different coarseness levels of coconut husks: coarse-grained and fine-grained. Initially, PTFE functioned as a dielectric and rotating component, making full physical contact with the static element which is the coconut husk.

Based on Figure 2, the sliding mode utilizes a stator and rotor each measuring 10 cm, operating in rotational motion. The stator houses positive charges on the coconut husk layer and negative charges on the electrode, enabling charge transfer for the sliding mechanism. In the initial stage, as the rotator turns, friction arises between the biomaterial film and either the PTFE plate or coconut husk plate, generating opposite charges due to their distinct triboelectric polarities. During this stage, the B-TENG does not experience electron flow. There is no charge transfer between the two plates in the initial state, so there is no electric potential [18].

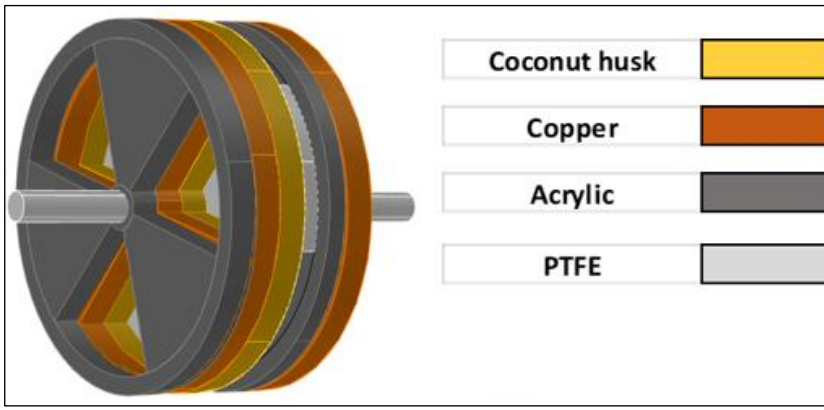

Figure 1: The multiple layers of B-TENG which the colour indicates the materials for both stator and rotor

In the second stage, when a gap forms between the coconut husk film and the PTFE plate, the inability to compensate for the triboelectric charges induces electron flow between the copper electrodes through electrostatic induction in the B-TENG. This generates output voltage and current signals. The third stage sees a continuous flow of electrons in the B-TENG until the gap distance reaches its maximum. At this point, reversed current/voltage signals occur when the same area of PTFE contacts the biomaterial, leading to the fourth stage. When the top plate is pressed, electrons transfer from the positive to the negative material, and upon load removal, the two plates separate, establishing an electric potential difference between them. In the fourth stage, the flow of electrons is repeated as same as the second stage process and as a result, Vac (Voltage alternate current) output signals are developed in the B-TENG. During the fifth stage, the maximum current flow is achieved, and the operating principle is repeated based on the first step. This process allows the B-TENG to produce Vac output signals in a repetitive cycle.

Measurement and characterization

Based on Figure 3, the dimension of B-TENG for different numbers of vanes with 10 cm of diameter and 0.8 cm for inner diameter specifically for shaft for both stator and rotor. The B-TENG with 3-vane has 60^{o} for each segment, while 45^{o} for 4-vane and 36^{o} for 5-vane. This experiment determined the output based on the effective area of TENG. Enhancing the performance of TENG can be effectively achieved through the augmentation of the actual contact area between frictional layers, leading to the generation of higher local pressure. The incorporation of micro or nanostructures serves this purpose, significantly increasing the density of triboelectric charges [22]-[23].

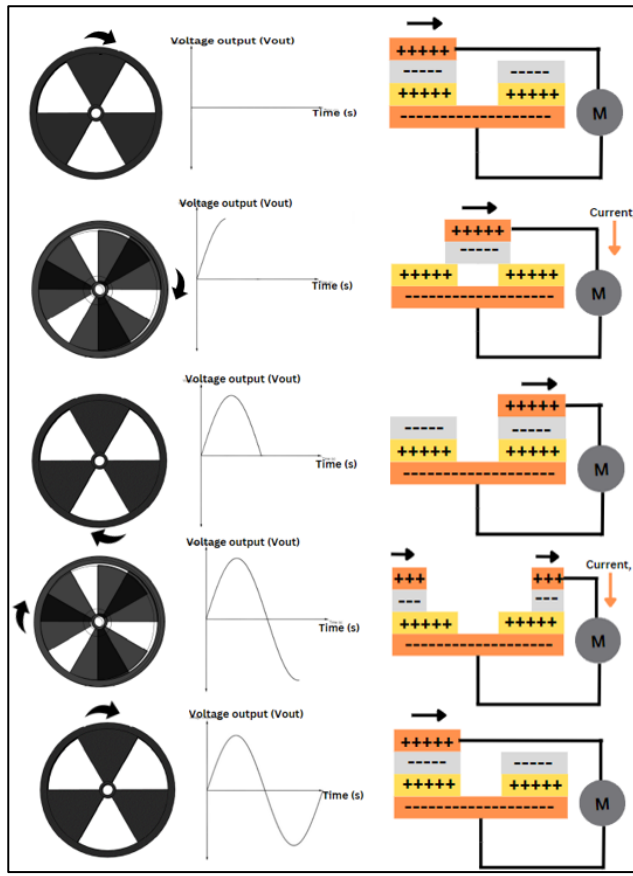

Figure 2: The working principle of B-TENG is based on sliding mode from phase 1 to phase 5

The angle of the sectors varies depending on the number of vanes for each B-TENG and is found by dividing 360° by the number of vanes per sample. The effective area which is represented by the shaded region depicted in Figure 3 can be calculated by using Equation (1). The r_1 represents the radius for the whole TENG, while r_2 for the small circle in the middle of TENG, and r_3 is the radius of the sector of B-TENG. According to Table 1, the 3-vane configuration exhibits a larger effective area for each vane compared to both the 4-vane and 5-vane configurations. Consequently, a smaller vane area concentrates charges more densely over a reduced surface area, leading to increased voltage output.

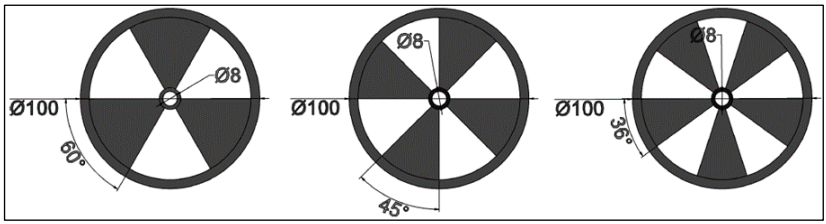

(a)

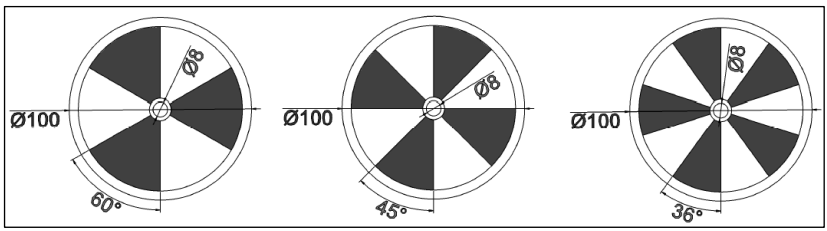

(b)

Figure 3: Dimension of B-TENG for each of vanes; (a) stator and (b) rotor

Using Equation (1) and Equation (2), the total effective area of the stator for each type of vane is 46.23 cm^2 and 31.56 cm^2 for the rotor as stated in Table 2. Even though the B-TENG comprises a variety number of vanes for each sample, the sum of the effective area is the same for all the vanes for both stator and rotor due to the same total angle of the shaded region accumulated. This leads to the same effective area with a number of vanes as the manipulated variables.

$$A_{total\ effective,stator} = \pi {r_1}^2 - \pi {r_2}^2 - n\left(\frac{\theta}{360} \times \pi {r_3}^2\right) \quad (1)$$

$$A_{total\ effective,rotor} = \frac{\pi {r_3}^2 - \pi {r_2}^2}{2} \quad (2)$$

where r_1 = 5 cm, r_2 = 0.4 cm, and r_3 = 4.5 cm.

Table 1: Effective area for both stator and rotor for different vanes

Properties	**Effective area for each vane or gap (cm^2)**	
	Stator	**Rotor**
3-vane	15.41	10.52
4-vane	11.56	7.89
5-vane	9.25	6.31

Table 2: Total effective area for both stator and rotor for different vanes

Total effective area (cm^2)	
Stator	**Rotor**
46.23	31.56

Equation (3) shows how the general voltage-charge (V-Q) relationship and Ohm's law can be used together to perform the resistive analysis where *R*, *C*, and V_{OC} are the external resistor, capacitance value, and open-circuit voltage respectively [31].

$$V_{charge} = R\frac{dQ}{dt} = \frac{-1}{C}Q + V_{oc} \tag{3}$$

Equation (4), the thickness of the triboelectric films is insignificant compared to other directions, the theory of parallel plates can be used to present the capacitance formulation. Where *A* is the total contact area of all segmentations; d_1 and d_2 are the thickness of the triboelectric layers, and ε_0 shows the absolute dielectric permittivity [32].

$$C = \frac{\varepsilon_0 A}{\frac{d_1}{\delta_1} + \frac{d_2}{\delta_2} + h} \tag{4}$$

However, the edge effects have been ignored. Considering the position of the top triboelectric layer, the contact area can be calculated on Equation (5) where ${r_2}^2$ and ${r_1}^2$ denote the inner and outer radius of the disk and return the absolute positive value [33].

$$A_{contact} = \frac{|\theta_0 - \theta|({r_2}^2 - {r_1}^2)}{2} \tag{5}$$

Then, because the output power of B-TENG varies concerning time, the average power is used in the calculations on Equation (6) where the time-varying electric field, together with the material's dielectric polarization and the tiny, time-varying movements of atomic bound charges, affects the displacement current [31].

$$P_{ave} = \frac{\int_0^T VI\,dt}{T} = \frac{\int_0^T RI^2\,dt}{T} \tag{6}$$

Consequently, using the parallel-plate capacitor model, the following equation can be used to estimate the total capacitance, *C* based on Equation (7). Where d_0 is the effective dielectric's thickness, w is the angular velocity

(rotation speed in rpm), *C* represents the total capacitance, *l* is the length of the board, and *x* is the gap distance or thickness. As in sliding mode, the two separate films with the back electrodes completely intersect at first. They each have positive and negative charges as a result of their different capacities for gaining and losing electrons. The contact area between the two materials decreases as it slides outward, resulting in the separation of charges in the plane and the generation of a potential difference [34].

$$C_{total} = \frac{\varepsilon_0 w(l-x)}{d_0} \tag{7}$$

The V_{oc} can be calculated based on Equation (8) where σ represents charge density, d_0 stands for effective thickness constant, x is for non-overlapped length, ε_0 stands for vacuum dielectric constant or permittivity (8.85×10^{-12} Fm^{-1}), and *I* is the board length or the outer circle perimeter. The average surface charge density of the dielectric layer was calculated and is 2.363×10^{-8}. The average dielectric layer surface charge density is assumed to be constant.

$$V_{OC} = \frac{\sigma x d_0}{\varepsilon_0 (I-x)} \tag{8}$$

By substituting Equation (3) into Equation (4), the *V-Q- x* relationship for the dielectric-to-dielectric B-TENG sliding mode is obtained. So, the average theoretical output voltage can be calculated using the following Equation (9).

$$V_{Theoretical} = -\frac{1}{C}Q + V_{OC} = \frac{d_0}{w\varepsilon_0(l-x)}Q + \frac{\sigma d_0 x}{\varepsilon_0(l-x)} \tag{9}$$

The experimental output voltage is determined by totaling the average output speed for all attempts. It can be determined by using Equation (10).

$$V = \frac{V_{1oc} + V_{2oc} + V_{3oc} + V_{4oc} + V_{5oc}}{5} \tag{10}$$

The find slope output voltage is determined by using the equation of polynomial where x is the speed of the motor from minimum to maximum output. It can be determined by using Equation (11).

$$ax^2 + bx + c = 0 \tag{11}$$

Table 3 shows the basic parameters used to determine the average surface charge density, σ, and the theoretical voltage for conductor to dielectric mode which is the control data for rotary sliding mode B-TENG.

Table 3: Basic parameter

Parameters	Value
ε_0	8.85×10^{-12} Fm^{-1}
Thickness constant, d	0.33
Non-overlapped length, x	$2 \times \pi \times 0.045$ m
Outer circle perimeter, I	0.62 m
Transferred charge, Q	1.5×10^{-12}
Length of dielectric, *l*	0.1 m
Width of dielectric, w	0.1 m

Methods

The experimental setup for characterizing the B-TENG's power output is illustrated in Figure 4. Several components need to be included in the experiment for the sliding mode mechanism. The setup includes several components subjected to various mechanical inputs, controlled by a speed controller, ranging from 200 RPM to 1400 RPM for the motor rotation speed and the speed indicator provides the tracking for current speed adjustment. The stator and rotor are accurately positioned to ensure proper contact between them. Additionally, the output voltage is measured using a data-measuring system. To evaluate the power output performance of the B-TENG, it is essential to characterize the device across a range of load resistances. The load can be represented by a variable resistor and a self-powered sensor module. Optimal power generation occurs under specific loading conditions, and the power density of the B-TENG can be determined based on the output power. The measurements comprise recording the average voltage for different vane configurations (3-vane, 4-vane, and 5-vane) using both fine-grained and coarse-grained coconut husks. Once the Highest voltage for the B-TENG is determined, the performance of the coconut husk layer can be assessed by applying loads to the B-TENG, ranging from 10 ohms to 20 k ohms.

Results and Discussion

The experiment's results and discussion encompass several key analyses: examining the relationship between speed and output voltage, comparing theoretical and experimental voltage outputs, estimating surface charge density, and conducting a comparison with prior studies while evaluating power density. The comparison between theoretical and experimental voltage aims to gauge their agreement in TENG operation. Estimation of surface

charge density is crucial for understanding its impact on TENG performance, derived from experimental data and equations. Additionally, comparing findings with previous research and assessing power density provides insights into advancing and optimizing TENG technology performance.

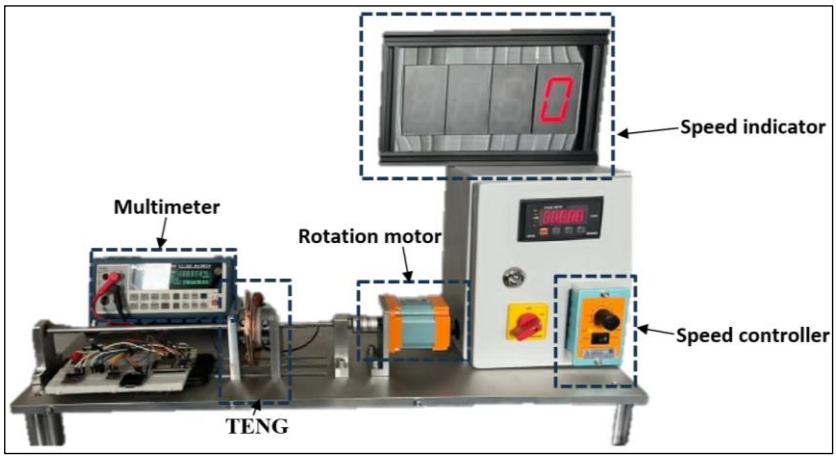

Figure 4: Experimental setup for sliding mode

Speed versus output voltage

The averages of output values were calculated based on the data shown in both Figure 5 and Figure 6. In each subsequent test, the rotational speed was systematically increased by 200 RPM to investigate how different speeds affect the output voltage. Specifically, at a motor speed of 1400 RPM, the open-circuit voltage (V_{OC}) exhibited a peak value of 4.00 V for configurations featuring a 5-vane. This was followed by measurements of 3.90 V and 3.68 V for configurations with 4-vane and 3-vane, respectively. The intricate relationship between the voltage response and the count of vanes underscored the nuanced impact of geometric variables on performance. This observation is substantiated by the empirical data presented in Figure 5. In contrast, the voltage response of coarse-grained coconut husk combined with PTFE displayed a distinct profile. Operating consistently at 1400 RPM, the configurations involving 5-vane, 4-vane, and 3-vane yielded maximum V_{OC} values of 3.45 V, 3.08 V, and 2.87 V, respectively. These findings, meticulously illustrated in Figure 6, accentuated the complex interplay between material properties and geometric arrangement, elucidating their combined influence on shaping the electrical performance of the B-TENG.

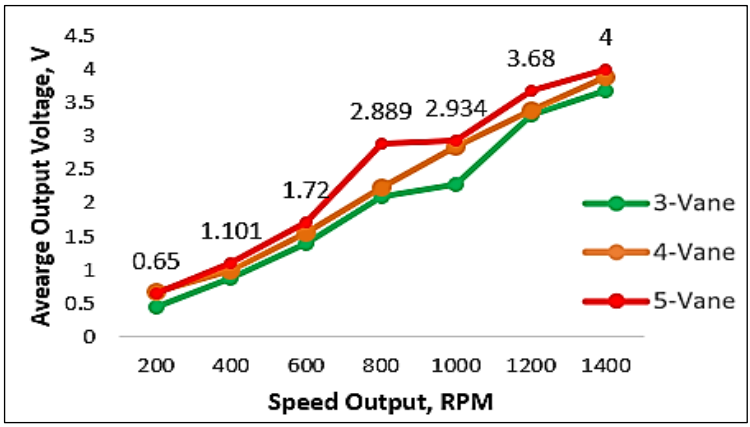

Figure 5: Average output voltage on the open circuit output voltage (V) for fine-grained coconut husk with PTFE

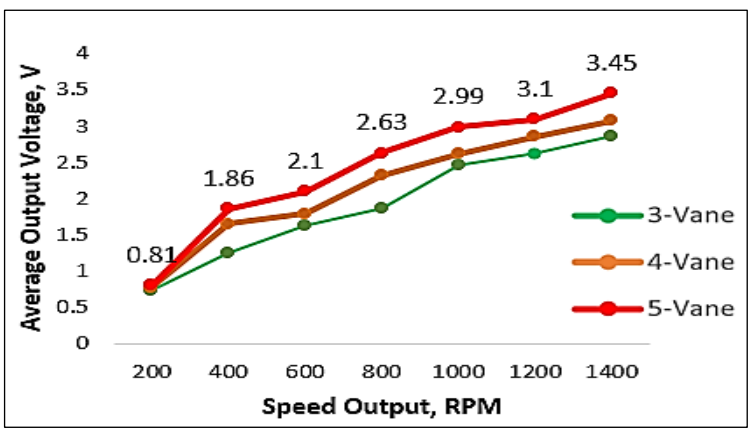

Figure 6: Average output voltage on the open circuit Output voltage (V) for coarse-grained coconut husk with PTFE

Theoretical voltage versus experimental voltage

Based on the data presented in Table 4, Table 5, and Table 6, it is evident that as the RPM increases, both the theoretical output voltage and the experimental output voltage show a corresponding increase. This observation indicates a positive correlation between RPM and the generated voltages. The finer-grained data provides additional insights, revealing that higher rotational speeds result in higher theoretical and experimental output voltages within the system. The theoretical output voltage is calculated using Equation (9), with

the fixed average surface charge density, while the voltage experimental is obtained using Equation (10). The percentage difference was calculated based on the theoretical and experimental voltages for fine and coarse-grained, respectively.

In Table 4, the highest percentage difference (%) occurs at 200 RPM for the fine-grained data, with a value of 32.50%, and for the coarse-grained data at 1400 RPM, with a value of 31.70%. In Table 5, the highest percentage difference (%) is observed at 200 RPM for the fine-grained data, reaching 23.15%, and for the coarse-grained data, it is at 200 RPM, with a value of 37.03%. Lastly, in Table 6, the highest percentage difference (%) is recorded at 200 RPM for the fine-grained data, measuring 39.32%, and for the coarse-grained data, it is at 200 RPM, with a value of 33.33%. Overall, the data from these tables consistently demonstrates that increasing RPM leads to higher theoretical and experimental output voltages, with varying degrees of percentage difference depending on the granularity of the data and rotational speed. The percentage difference between 200 RPM and 1400 RPM leads to the highest number of differences.

Table 4: Percentage difference between theoretical and experimental voltage output for 3-vane

Speed (RPM)	Theory (Volt)	Fine-grained		Coarse-grained	
		Experiment (Volt)	Diff (%)	Experiment (Volt)	Diff (%)
200	0.54	0.80	32.50	0.73	26.02
400	1.08	0.88	22.72	1.26	14.28
600	1.62	1.38	17.39	1.62	0.10
800	2.16	2.09	3.34	1.86	16.12
1000	2.70	2.29	17.90	2.46	9.75
1200	3.24	3.32	2.40	2.63	23.19
1400	3.78	3.68	2.71	2.87	31.70

Estimation of surface charge density

Enhancing the output power density of TENGs is pivotal, as empirical evidence reveals a quadratic relationship with their surface charge density (σ) [24]. Based on experimental findings, the charge density serves as sigma, and the surface charge density (σ) can be estimated using Equation (10) and Equation (11) alongside experimental data.

Table 5: Percentage difference between theoretical and experimental voltage output for 4-vane

Speed (RPM)	Theory (Volt)	Fine-grained		Coarse-grained	
		Experiment (Volt)	Diff (%)	Experiment (Volt)	Diff (%)
200	0.54	0.85	23.15	0.74	37.03
400	1.08	0.98	9.17	1.28	18.51
600	1.62	1.56	3.21	1.79	10.49
800	2.16	2.22	3.10	2.32	7.40
1000	2.70	2.85	5.78	2.62	2.96
1200	3.24	3.40	5.09	2.86	11.72
1400	3.78	3.90	3.17	3.08	18.51

Table 6: Percentage difference between theoretical and experimental voltage output for 5-vane

Speed (RPM)	Theory (Volt)	Fine-grained		Coarse-grained	
		Experiment (Volt)	Diff (%)	Experiment (Volt)	Diff (%)
200	0.54	0.89	39.32	0.81	33.33
400	1.08	1.10	1.81	1.21	10.74
600	1.62	1.72	5.81	2.10	22.85
800	2.16	2.88	25.00	2.63	17.87
1000	2.70	2.93	7.84	2.99	9.68
1200	3.24	3.68	11.95	3.10	4.51
1400	3.78	4.00	5.50	3.45	9.56

Analysis of data presented in Tables 7, 8, and 9 reveals an increment pattern, particularly noteworthy is the gradual increment in experimental voltage measurements correlating with speed, reaching a peak at maximum speed. Sigma values derived from Table 7 indicate a significant disparity, with coarse-grained data yielding a sigma of 3.35E-08 compared to 3.25E-08 for fine-grained data. Similar trends are observed in Tables 8 and 9, with the most substantial sigma values appearing in fine-grained data which is 3.41E-08 for 4-vane and 3.64E-08 for 5-vane while for coarse-grained 2.96E-08 for 4-vane and 2.23E-08 for 5-vane. Notably, the discrepancies in sigma values greatly impact the percentage disparity between theoretical and experimental output voltage, underscoring the importance of even minor differences in empirical sigma values. This emphasis on identifying significant disparities is crucial for accurate analysis, given the amplified contrasts resulting from minor discrepancies in smaller empirical sigma values.

Table 7: Sigma for 3-vane for fine-grained and coarse-grained

Speed (RPM)	Sigma (Fine-grained)	Sigma (Coarse-grained)
200	7.08E-09	5.35E-09
400	7.78E-09	1.01E-08
600	1.22E-08	1.41E-08
800	1.84E-08	1.91E-08
1000	2.02E-08	2.39E-08
200	2.93E-08	2.87E-08
1400	3.25E-08	3.35E-08

Table 8: Sigma for 4-vane for fine-grained and coarse-grained

Speed (RPM)	Sigma (Fine-grained)	Sigma (Coarse-grained)
200	6.20E-09	6.73E-09
400	9.61E-09	1.10E-08
600	1.45E-08	1.47E-08
800	1.93E-08	1.84E-08
1000	2.42E-08	2.21E-08
200	2.92E-08	2.58E-08
1400	3.41E-08	2.96E-08

Table 9: Sigma for 5-vane for fine-grained and coarse-grained

Speed (RPM)	Sigma (Fine-grained)	Sigma (Coarse-grained)
200	6.05E-09	7.43E-09
400	1.18E-08	1.35E-08
600	1.73E-08	1.81E-08
800	2.25E-08	2.12E-08
1000	2.74E-08	2.30E-08
200	3.21E-08	2.34E-08
1400	3.64E-08	2.23E-08

Comparison with previous work and power density

TENG typically consists of friction materials, conductive materials, and base materials. These devices capture environmental mechanical energy and offer distinct advantages, including high efficiency, a straightforward structure, and compatibility with various materials. Table 10 summarizes the current characteristics associated with materials derived from general bio-based sources, particularly bio-based material, in the context of TENGs. The coconut husk generates a substantial output compared to other materials such as corn [25], eggshell [26], CNF [27], leaves [28], and Methyl-CNF [29]. This approach supports the environmentally friendly and large-scale production of TENGs. Utilizing 5-vane fine-grained coconut husks as an essential

component. This configuration stands out as a leading candidate for material selection, based on power output and density parameters. Following this success, a subsequent iteration of the experiment was conducted, involving a configuration with the 5-vane ingeniously crafted from fine-grained coconut husks. This phase aimed to maximize power output by measuring the voltage across various resistances. The culmination of these efforts is summarized in Table 11 outlining chosen resistances and corresponding power levels. Notably, the peak power output of 121.10 mW was achieved with a resistance of 10 Ω. This peak power output was then used to calculate the power density in the sliding mode experiment in Table 12 highlighting the interplay between material characteristics and operational parameters. By dividing the maximum power by the sliding system's surface area of 31.56 cm^2, a remarkable power density of 3.84 mW/cm^2 was calculated. This value underscores the effectiveness and potential of this innovative configuration in achieving high power densities within a compact design.

Table 10: Difference bio-based materials with its output performance

Ref.	Bio-materials	Active	Output performance (V)
This work	Coconut husk	PDMS	4
[24]	Corn	PDMS	10
[25]	Egg Shell	PTFE	15.8
[26]	CNF	FEP	5
[27]	Leaves	PMMA	10
[28]	Methyl-CNF	Nitro-CNF	8

Table 11: Measuring current across the resistor using the highest output voltage from fine-grained coconut husk with different load resistance

Resistance (Ω)	Current (mA)	Power (mW)
10	3.480	121.10
47	0.751	26.51
150	0.232	8.07
330	0.111	4.07
510	0.075	2.87
1000	0.035	1.22
2000	0.026	1.35
3000	0.022	1.45
4700	0.018	1.52
6000	0.016	1.54
10000	0.011	1.21
20000	0.007	0.98

Table 12: Peak power and power density

Peak power (mW)	Surface area (cm^2)	Power density
121.10	31.56	3.84

Conclusion and Future Works

The exploration of coconut waste as a biomaterial for nano-powered sensors within the framework of B-TENG has yielded promising results. Motivated by the global need for sustainable energy solutions, this study focused on characterizing coconut waste-derived B-TENG and understanding its working principles. The experiment involved phases from preparing coconut waste to exploring the sliding mode mechanism in B-TENG. The integration of coconut waste into energy-harvesting devices offers extensive benefits over conventional synthetic materials, given its abundance and renewable nature. The study achieved significant objectives, including assessing the effects of coconut waste variations, motor speed fluctuations, and vane count on B-TENG performance. The 5-vane configuration demonstrated a positive correlation between vane count and performance. Optimizing biomaterial thickness, vane design, and material refinement can further boost performance [30].

Noteworthy findings include achieving the highest average voltage of 4 V and optimal power density of 3.84 mW/cm² at a 10 Ω load. These results, obtained with finely textured coconut husk and a 5-vane configuration, underscore the potential for performance improvement through biomaterial thickness, vane design, and material refinement. This research highlights coconut waste as a versatile biomaterial with substantial implications for enhancing B-TENG performance, particularly in powering low-energy applications. The experiment underscores the vast capacity of coconut waste as an unlimited and renewable resource in the realm of energy harvesting, presenting opportunities for enduring and highly effective energy solutions.

Contributions of Authors

The authors confirm the equal contribution in each part of this work. All authors reviewed and approved the final version of this work.

Funding

This work was supported by the “application form fundamental research grant scheme (FRGS)” [FRGS/1/2020/TK0/UNITEN/01/2, Characterisation of Bio-

Based Triboelectric Nanogenerator (B-TENG) for Self-Powered Sensor Applications and 2020].

Conflict of Interests

All authors declare that they have no conflicts of interest.

Acknowledgement

This work was supported by the Ministry of Higher Education, Malaysia, through the Fundamental Research Grant Scheme (FRGS), under project code FRGS/1/2020/TK0/UNITEN/01/2.

References

[1] C. Ligeikis, A. Bouma, J. Shim, S. Manzato, R. J. Kuether, and D. R. Roettgen, "Modeling and experimental validation of a pylon subassembly mockup with multiple nonlinearities," *Conference Proceedings of the Society for Experimental Mechanics*, vol. 1, pp. 59–74, 2021. doi: 10.1007/978-3-030-47626-7_10

[2] P. Górski, M. Napieraj, and E. Konopka, "Variability evaluation of dynamic characteristics of highway steel bridge based on daily traffic-induced vibrations", *IEEE Transactions on Instrumentation and Measurement*, vol. 164, pp. 1–20, 2020. doi: 10.1016/j.measurement.2020.108074

[3] S. Sunithamani, S. Arunmetha, B. Poojitha, A. Niveditha, B. Ankitha, and P. Lakshmi, "Performance study of teng for energy harvesting application," *Journal of Physics: Conference Series*, vol. 2471, no. 1, pp. 1-9, 2023. doi: 10.1088/1742-6596/2471/1/012022

[4] Y. Wang, J. Zhang, X. Jia, M. Chen, H. Wang, G. Ji, H. Zhou, Z. Fang, and Z. Gao, "TENG-based self-powered device - The heart of life," *Nano Energy*, vol. 119, pp. 1-23, 2024. doi: 10.1016/j.nanoen.2023.109080

[5] A. Baburaj, S. K. Naveen Kumar, A. K. Aliyana, M. Banakar, S. Bairagi, and G. Stylios, "Factors affecting the performance of flexible triboelectric nanogenerators (F-TENGs) and their sensing capabilities: A comprehensive review," *Nano Energy*, vol. 118, pp. 1-23, 2023. doi: 10.1016/j.nanoen.2023.108983

[6] M. K. Azwan and H. Salleh, "Development of hybrid contact mode triboelectric and electromagnetic energy harvester," *International Journal of Recent Technology and Engineering*, vol. 8, no. 4, pp. 1652-1656, 2019. doi: 10.35940/ijrte.D5101.118419

[7] X. Wang, W. Tong, R. Yu, J. Zhang, Y. Liu, C. Gao, Y. Zhang, Z. Wang, S. Liu, Q. An, and Y. Zhang, "Mica's homo-positive-charging behavior enabled porous elastomer TENG for energy harvesting in high humidity", *Nano Energy*, vol. 119, pp. 1-10, 2024. doi: 10.1016/j.nanoen.2023.109056

[8] R. Walden, C. Kumar, D. M. Mulvihill, and S. C. Pillai, "Opportunities and challenges in triboelectric nanogenerator (TENG) based sustainable energy generation technologies: A mini review," *Chemical Engineering Journal Advances*, vol. 9, p. 100237, 2022. doi: 10.1016/j.ceja.2021.100237

[9] S. R. Ganapathy, H. Salleh, and M. K. A. Azhar, "Design and optimization of magnetically-tunable hybrid piezoelectric-triboelectric energy harvester", *Scientific Reports*, vol. 11, no. 1, pp. 1-13, 2019. doi: 10.1038/s41598-021-83776-y

[10] X. Dong, F. Liu, L. Wang, L. Xu, H. Pan, and J. Qi, "Nano-generators for biomedical applications", *Materials Today Communications*, vol. 35, p. 105493, 2023. doi: 10.1016/j.mtcomm.2023.105493

[11] K. Y. Song, S. W. Kim, D. C. Nguyen, J. Y. Park, T. T. Luu, D. Choi, J. M. Baik, and S. An, "Recent progress on nature-derived biomaterials for eco-friendly triboelectric nanogenerators", *EcoMat*, vol. 5, no. 8, pp. 1-27, 2023. doi: 10.1002/eom2.12357

[12] D. Anand, S. Sambyal, and R. Vaid, "Triboelectric nanogenerators (TENG): Factors affecting its efficiency and applications", *Facta Universitatis - Series: Electronics and Energetics*, vol. 34, no. 2, pp. 157–172, 2021.

[13] Y. Pan, M. Li, T. Huang, X. Hao, M. Lu, S. Chen, K. Zhang, and A. Qin, "Dynamic co-irradiation techniques: A new method improving the electrical output of TENG by optimizing the charge capture capacity of polypropylene membrane", *Applied Materials Today*, vol. 35, pp. 1-9, 2023. doi: 10.1016/j.apmt.2023.101979

[14] K. Thinkohkaew, N. Rodthongkum, and S. Ummartyotin, "Coconut husk (Cocos nucifera) cellulose reinforced poly vinyl alcohol-based hydrogel composite with control-release behavior of methylene blue," *Journal of Materials Research and Technology*, vol. 9, no. 3, pp. 6602–6611, 2020. doi: 10.1016/j.jmrt.2020.04.051

[15] F. Gaspar, A. Bakatovich, N. Davydenko, and A. Joshi, "Building insulation materials based on agricultural wastes", in *Bio-Based Materials and Biotechnologies for Eco-Efficient Construction*, Woodhead Publishing, 2020, pp. 149–170.

[16] K. Nanthagal, S. Khoonsap, V. Harnchana, P. Suphasorn, N. Chanlek, K. Sinthiptharakoon, K. Lapawae, and S. Amnuaypanich, "Unprecedented triboelectric effect of lignin on enhancing the electrical outputs of natural-rubber-based triboelectric nanogenerators (TENGs)", *ACS Sustainable Chemistry and Engineering*, vol. 11, no. 4, pp. 1311–1323, 2023. doi:

10.1021/acssuschemeng.2c03197
[17] N. R. Tanguy, M. Rana, A. A. Khan, X. Zhang, N. Tratnik, H. Chen, D. Ban, and N. Yan, "Natural lignocellulosic nanofibrils as tribonegative materials for self-powered wireless electronics", *Nano Energy*, vol. 98, pp. 1-11, 2022. doi: 10.1016/j.nanoen.2022.107337
[18] H. Mohd, M. Zakaria, M. Zaffrie, M. Amin, A. Faireal, M. Syafiq, A. Dani, M. H. Zakaria, M. Zaffrie, M. Amin, and M. F. Ahmad, "Market potential and competitiveness assessment of Malaysian coconut-based products (Potensi pasaran dan penilaian daya saing produk berasaskan kelapa di Malaysia)", *Economic and Technology Management Review*, vol. 18, pp. 11–22, 2022.
[19] S. Lu, L. Gao, X. Chen, D. Tong, W. Lei, P. Yuan, X. Mu, and H. Yu, "Simultaneous energy harvesting and signal sensing from a single triboelectric nanogenerator for intelligent self-powered wireless sensing systems", *Nano Energy*, vol. 75, pp. 1-11, 2020. doi: 10.1016/j.nanoen.2020.104813
[20] K. Dong, X. Peng, and Z. L. Wang, "Fiber/fabric-based piezoelectric and triboelectric nanogenerators for flexible/stretchable and wearable electronics and artificial intelligence", *Advanced Materials*, vol. 32, no. 5, pp. 1-43, 2020. doi: 10.1002/adma.201902549
[21] S. Lee, Q. Shi, and C. Lee, "From flexible electronics technology in the era of IoT and artificial intelligence toward future implanted body sensor networks", *APL Materials*, vol. 7, no. 3, pp. 1-13, 2019. doi: 10.1063/1.5063498
[22] W. Yang, X. Wang, H. Li, J. Wu, Y. Hu, Z. Li, and H. Liu, "Fundamental research on the effective contact area of micro-/nano-textured surface in triboelectric nanogenerator", *Nano Energy*, vol. 57, pp. 41–47, 2019. doi: 10.1016/j.nanoen.2018.12.029.
[23] Luo, Y., Li, Y., Feng, X., Pei, Y., Zhang, Z., Wang, L., Zhao, Y., Lu, B., & Zhu, B, "Triboelectric nanogenerators with porous and hierarchically structured silk fibroin films via water electrospray-etching technology", *Nano Energy*, vol. 75, pp. 1-9, 2020. doi: 10.1016/j.nanoen.2020.104974
[24] C. Zhang, L. Zhou, P. Cheng, X. Yin, D. Liu, X. Li, H. Guo, Z. L. Wang, and J. Wang, "Surface charge density of triboelectric nanogenerators: Theoretical boundary and optimization methodology", *Applied Materials Today*, vol. 18, pp. 1-8, 2020. doi: 10.1016/j.apmt.2019.100496
[25] C. Jiang, Q. Zhang, C. He, C. Zhang, X. Feng, X. Li, Q. Zhao, Y. Ying, and J. Ping, "Plant-protein-enabled biodegradable triboelectric nanogenerator for sustainable agriculture", *Fundamental Research*, vol. 2, no. 6, pp. 974–984, 2022
[26] J. Kaur, H. Singh, R. S. Sawhney, T. Sui, and U. Trdan, "Waste biomaterial-SnO nanoparticles composite based green triboelectric nanogenerator for self-powered human motion monitoring", *ACS Applied Electronic Materials*, vol. 4, no. 9, pp. 4694–4707, 2022. doi:

10.1021/acsaelm.2c00887

[27] C. Yao, A. Hernandez, Y. Yu, Z. Cai, and X. Wang, "Triboelectric nanogenerators and power-boards from cellulose nanofibrils and recycled materials", *Nano Energy*, vol. 30, pp. 103–108, 2016. doi: 10.1016/j.nanoen.2016.09.036

[28] Y. Jie, X. Jia, J. Zou, Y. Chen, N. Wang, Z. L. Wang, and X. Cao, "Natural leaf made triboelectric nanogenerator for harvesting environmental mechanical energy", *Advanced Energy Materials*, vol. 8, no. 12, pp. 1-7, 2018. doi: 10.1002/aenm.201703133

[29] C. Yao, X. Yin, Y. Yu, Z. Cai, and X. Wang, "Chemically functionalized natural cellulose materials for effective triboelectric nanogenerator development", *Advanced Functional Materials*, vol. 27, no. 30, pp. 1-7, 2017. doi: 10.1002/adfm.201700794

[30] M. A. Saparin, H. Salleh, C. K. Hen, and S. Kumar, "Comparison of bio-based triboelectric nanogenerator (B-TENG) performance for self-powered sensor applications," in *2023 3rd International Conference on Electrical, Computer, Communications and Mechatronics Engineering*, pp. 1-6, 2023. doi: 10.1109/iceccme57830.2023.10253340

[31] H. Zhang, L. Yao, L. Quan, and X. Zheng, "Theories for triboelectric nanogenerators: A comprehensive review", *Nanotechnology Reviews*, vol. 9, no. 1, pp. 610-625, 2020. doi: 10.1515/ntrev-2020-0049

[32] S. Niu, Y. Liu, S. Wang, L. Lin, Y. S. Zhou, Y. Hu, and Z. L. Wang, "Theory of sliding-mode triboelectric nanogenerators," *IEEE Transactions on Electron Devices*, vol. 65, no. 9, pp. 3851–3857, 2018. doi: 10.1002/adma.201302808

[33] J. Shao, T. Jiang, and Z. Wang, "Theoretical foundations of triboelectric nanogenerators (TENGs)", *Science China Technology Sciences*, vol. 63, pp. 1087–1109, 2020. doi: 10.1007/s11431-020-1604-9

[34] Z. L. Wang, L. Lin, J. Chen, S. Niu, and Y. Zi, "Triboelectric Nanogenerator: Lateral Sliding Mode," in *Triboelectric Nanogenerators, Green Energy and Technology*, Springer, Cham, 2016, pp. 49-82.